Tests of the PSF reconstruction algorithm for NACO/VLT

Yann Clénet[a,g], Christopher Lidman[d], Eric Gendron[b,g], Gérard Rousset[c,g],
Thierry Fusco[e], Nick Kornweibel[d], Markus Kasper[f], Nancy Ageorges[d]

[a]LESIA/CNRS, Observatoire de Paris, 5 place Jules Janssen, 92195 Meudon cedex, France;
[b]LESIA/Observatoire de Paris, 5 place Jules Janssen, 92195 Meudon cedex, France;
[c]LESIA/Université Paris Diderot, Observatoire de Paris, 5 place Jules Janssen, 92195 Meudon cedex, France;
[d]ESO, Alonso de Córdova, Casilla 3107, Vitacura, Casilla 19001, Santiago 19, Chile;
[e]ONERA, BP52, 29 avenue de la Division Leclerc, 92320 Châtillon Cedex, France;
[f]ESO, Karl-Schwarzschild-Strasse 2, D-85748 Garching bei München, Germany;

ABSTRACT

We have developed an PSF reconstruction algorithm for the NAOS adaptive optics system that is coupled with CONICA at ESO/VLT. We have modified the algorithm of Véran et al. (1997), originally written for PUEO at CFHT, to make use of the specific real-time wavefront-related data that observers with NACO receive together with their scientific images. In addition, we use the V_{ii} algorithm introduced by Clénet et al. (2006) and Gendron et al. (2006) instead of the U_{ij} algorithm originally used by Véran et al. (1997).

Until now, tests on NAOS has been undertaken during technical time thanks to the NACO team at Paranal. A first test has been successfully performed to calibrate the orientation of reconstructed PSFs with respect to NACO images. We have also obtained two sets of PSF reconstruction test data with NACO in November 2006 and September 2007 to reconstruct PSFs. Discrepancies exist between the observed and reconstructed PSFs: their Strehl ratios are $\sim$31% and $\sim$39% respectively in Nov. 2006, $\sim$31% and $\sim$19% respectively in Sept. 2007. These differences may be at least partly explained by reconstructions that either did not account for the aliasing contribution or poorly estimated the noise contribution with the available noise information at that time.

We have additionally just started to test our algorithm using the AO bench Sésame, at LESIA. Results are promising but need to be extended to a larger set of atmospheric conditions or AO correction qualities.

Keywords: Adaptive optics; NAOS-CONICA; PSF reconstruction; simulations; Sésame AO bench

1. INTRODUCTION

Point-Spread-Function (PSF) reconstruction is now a well-known PSF calibration method in adaptive optics (AO) imaging that allows one to overcome the spatial and temporal PSF variability: when classical imaging usually makes use of specific PSF acquisitions, in alternance with the scientific ones, AO imaging takes advantage of real-time wavefront-related data to reconstruct, off-line, the PSF. The benefit of the latter is in time spent on the scientific targets (the need for specific PSF acquisitions is almost suppressed) and in principle in calibration reliability (the reconstructed PSFs has "seen" the same atmospheric conditions as the corresponding scientific images).

The first, and most successful, development of a PSF reconstruction algorithm has been realised for PUEO at CFHT (Véran et al., 1997) and has been at the basis of further developments for various telescopes and AO systems: ADONIS at the ESO 3.6m telescope (Harder & Chelli, 2000), ALFA at the Calar Alto 3.5m telescope (Weiss, 2003), Altair at the Gemini North telescope (Jolissaint et al., 2004), the AO system of the UCO/Lick Observatory's 3 m Shane Telescope (Fitzgerald, 2004) and the AO system of the Keck telescope (Flicker et al., 2008).

On our side, we have written a PSF reconstruction algorithm for NAOS at VLT (Clénet et al., 2006) which is a modified version of the PUEO algorithm. In the following, we first briefly describe our algorithm, present our first on-sky tests, introduce our first laboratory AO bench tests and finally conclude on our perspectives.

2. DESCRIPTION OF THE ALGORITHM FOR NAOS

Except for new developments, we will give in this section only a brief description of the algorithm. Details can be found in previous publications (Clénet et al., 2006; Gendron et al., 2006).

2.1 The long-exposure AO-corrected PSF expression

Under the assumption of a quasi-stationnary phase over the pupil, the AO-corrected monochromatic long-exposure optical transfer function (OTF) can be written as follows:

$$\left\langle OTF(\vec{\rho}/\lambda) \right\rangle = \left\langle OTF_{\phi_\epsilon}(\vec{\rho}/\lambda) \right\rangle \times OTF_{\text{tel}}(\vec{\rho}/\lambda) \tag{1}$$

Decomposing the phase ϕ_ϵ over the space spanned by the mirror modes, $\phi_{\epsilon_\parallel}$, and over the space orthogonal to the latter, $\phi_{\epsilon_\perp}$, this equation becomes:

$$\left\langle OTF(\vec{\rho}/\lambda) \right\rangle = \left\langle OTF_{\phi_{\epsilon_\parallel}}(\vec{\rho}/\lambda) \right\rangle \times \left\langle OTF_{\phi_{\epsilon_\perp}}(\vec{\rho}/\lambda) \right\rangle \times OTF_{\text{tel}}(\vec{\rho}/\lambda) \tag{2}$$

From the relation between the phase structure function and the optical transfer function, we get:

$$\left\langle OTF(\vec{\rho}/\lambda) \right\rangle = \exp\left(-\frac{1}{2}\bar{D}_{\phi_{\epsilon_\parallel}}(\vec{\rho})\right) \times \exp\left(-\frac{1}{2}\bar{D}_{\phi_{\epsilon_\perp}}(\vec{\rho})\right) \times OTF_{\text{tel}}(\vec{\rho}/\lambda) \tag{3}$$

where:

- $\left\langle OTF_{\phi_\epsilon}(\vec{\rho}/\lambda) \right\rangle$ is the attenuation of the long-exposure OTF due to the partial correction of AO,

- $OTF_{\text{tel}}(\vec{\rho}/\lambda)$ is the perfect telescope OTF,

- $\left\langle OTF_{\phi_{\epsilon_\parallel}}(\vec{\rho}/\lambda) \right\rangle$ is the attenuation of the long-exposure OTF due the mirror component of the phase, i.e. the "residual parallel phase",

- $\left\langle OTF_{\phi_{\epsilon_\perp}}(\vec{\rho}/\lambda) \right\rangle$ is the attenuation of the long-exposure OTF due the component of the phase belonging to the space perpendicular to the mirror space, i.e. the "perpendicular phase",

- $\bar{D}_{\phi_{\epsilon_\parallel}}(\vec{\rho})$ is the mean structure function of the residual parallel phase,

- $\bar{D}_{\phi_{\epsilon_\perp}}(\vec{\rho})$ is the mean structure function of the perpendicular phase,

- $\vec{\rho}$ is a pupil plane coordinate vector, and

- λ is the wavelength of observation.

2.2 Expression of the mean structure function of the residual parallel phase

2.2.1 The $U_{ij}(\vec{\rho})$ and $V_{ii}(\vec{\rho})$ algorithms

In the classical PSF reconstruction algorithm developed by Véran et al. (1997), hereafter the "$U_{ij}(\vec{\rho})$ algorithm", after decomposing the residual parallel phase in the basis of the mirror modes $\{M_i(\vec{x})\}_{i=1...N}$:

$$\phi_{\epsilon_\parallel}(\vec{x}, t) = \sum_{i=1}^{N} \epsilon_{\parallel i}(t)\, M_i(\vec{x}) \tag{4}$$

$\bar{D}_{\phi_{\epsilon_\parallel}}(\vec{\rho})$ is expressed as a function of the U_{ij} functions:

$$\bar{D}_{\phi_{\epsilon_\parallel}}(\vec{\rho}) = \sum_{i=1}^{N} \sum_{j=1}^{N} \langle \epsilon_{\parallel i} \epsilon_{\parallel j} \rangle \, U_{ij}(\vec{\rho}) \tag{5}$$

where the $U_{ij}(\vec{\rho})$ functions are defined by:

$$\frac{\int \left(M_i(\vec{x}) - M_i(\vec{x} + \vec{\rho}) \right) \left(M_j(\vec{x}) - M_j(\vec{x} + \vec{\rho}) \right) P(\vec{x}) P(\vec{x} + \vec{\rho}) \mathrm{d}\vec{x}}{\int P(\vec{x}) \, P(\vec{x} + \vec{\rho}) \mathrm{d}\vec{x}}, \tag{6}$$

with $P(\vec{r})$ the pupil function and $\vec{x}$ a coordinate vector in the pupil plane.

In the $V_{ii}(\vec{\rho})$ algorithm, we work with the basis that diagonalises the residual parallel phase covariance matrix $\langle \epsilon_\parallel \epsilon_\parallel{}^t \rangle$:

$$\Lambda = B^t \langle \epsilon_\parallel \epsilon_\parallel{}^t \rangle B, \tag{7}$$

where Λ is a diagonal matrix that contains the $\{\lambda_i\}_{i=1...N}$ eigenvalues and B is the matrix of eigenvectors: $B^t B = BB^t = Id$. In this new basis, the mean residual parallel phase structure function reduces to:

$$\bar{D}_{\phi_{\epsilon_\parallel}}(\vec{\rho}) = \sum_{i=1}^{N} \langle \eta_i \eta_i \rangle \, V_{ii}(\vec{\rho}) = \sum_{i=1}^{N} \lambda_i \, V_{ii}(\vec{\rho}), \tag{8}$$

where the $V_{ij}(\vec{\rho})$ functions are the equivalent in the new basis to the $U_{ij}(\vec{\rho})$ functions (Eq. 5). Similarly to Eq. 6, the $V_{ij}(\vec{\rho})$ functions are defined by

$$\frac{\int \left(M_i'(\vec{x}) - M_i'(\vec{x} + \vec{\rho}) \right) \left(M_j'(\vec{x}) - M_j'(\vec{x} + \vec{\rho}) \right) P(\vec{x}) P(\vec{x} + \vec{\rho}) \mathrm{d}\vec{x}}{\int P(\vec{x}) \, P(\vec{x} + \vec{\rho}) \mathrm{d}\vec{x}}, \tag{9}$$

such that $\mathcal{M}'$, the matrix made of the eigenvector modes $\{M_i'(\vec{x})\}_{i=1...N}$, is given by $\mathcal{M}' = B^t \mathcal{M}$, $\mathcal{M}$ being the matrix made of the mirror modes $\{M_i(\vec{x})\}_{i=1...N}$.

A large amount of disk space is saved using the V_{ii} functions since they are computed on the fly whereas the U_{ij} need to be saved on a disk. Moreover, the U_{ij} and V_{ii} algorithms mathematically produce the same OTFs and in our tests, the latter has demonstrated a huge gain, a factor 25!, in computation time. Since NACO does not deliver to the observer the complete slope and voltage measurements recorded during an exposure but the covariance matrices corresponding to these measurements, our PSF reconstruction algorithm for NACO highly benefits from this V_{ii} algorithm.

2.2.2 Computation of the $\langle \epsilon_\parallel \epsilon_\parallel{}^t \rangle$ matrix

In the PSF reconstruction algorithms derived from Véran et al. (1997), the covariance matrix $\langle \epsilon_\parallel \epsilon_\parallel{}^t \rangle$ is basically the entry point from which one can deduce successively the phase structure function, the OTF, and then the PSF. Assuming a sufficiently high temporal bandwidth, this covariance matrix is decomposed as follows:

$$\langle \epsilon_\parallel \epsilon_\parallel{}^t \rangle = \langle \hat{\epsilon}_\parallel \hat{\epsilon}_\parallel^t \rangle - \langle nn^t \rangle + \langle rr^t \rangle \tag{10}$$

where $\langle \hat{\epsilon}_\parallel \hat{\epsilon}_\parallel^t \rangle$, $\langle nn^t \rangle$ and $\langle rr^t \rangle$ are the covariance matrices of the WFS measurement, noise and aliasing, respectively.

When observing with NACO, any resulting scientific FITS image is provided together with the covariance of the modal coefficients deduced from the residual slopes ($C_{\epsilon\epsilon}$), the mean of the modal coefficients deduced from the residual slopes ($\bar{\epsilon}$), computed during the image acquisition. The WFS measurement covariance matrix can be directly computed from these data: $\langle \hat{\epsilon}_\parallel \hat{\epsilon}_\parallel^t \rangle = C_{\epsilon\epsilon} - \langle \bar{\epsilon}\bar{\epsilon}^t \rangle$.

Similarly, the Zernike mean noise $\overline{n_z^2}$, computed during the image acquisition from the autocorrelation of the slopes projected on the Zernike basis (Fusco et al., 2004), was given in any scientific image FITS header. Since After a recent slight modification of the NAOS real-time controller (RTC) software, this is now the whole vector of variance noise $n_{z_i}^2$ for all considered Zernikes that is delivered inside any scientific image FITS header.

The aliasing covariance matrix is computed using a Shack-Hartmann simulation and a Zernike mode basis, using a large number of mode: we compute the difference between the projection of the Zernikes on the NAOS modes and this same projection after the Zernikes being seen by the WFS. This computation being made at $D/r_0=1$, it is then scaled at the proper D/r_0 value, r_0 being taken in the scientific image FITS header (Fusco et al., 2004), and the aliasing covariance matrix is then given by:

$$\langle nn^t \rangle = \left(\frac{D}{r_0}\right)^{\frac{5}{3}} \left(D_M^+ D_Z^\infty - P_{ZM}^\infty\right) C_{Noll} \left(D_M^+ D_Z^\infty - P_{ZM}^\infty\right)^t \tag{11}$$

where D^+ is the modal command matrix, D_Z^∞ is the interaction matrix on the Zernike modes simulated with a large number of Zernikes and P_{ZM}^∞ is the projector of the Zernike modes on the system modes (always considering a large number of Zernike modes). For NAOS, we have considered 903 Zernike modes.

2.3 Expression of the mean structure function of the perpendicular phase

Using the perpendicular part $\phi_{\epsilon_\perp}(\vec{x}, t)$ of a large number simulated phase screens, the mean structure function of the perpendicular phase is computed with the following equation (Clénet et al., 2006) :

$$\bar{D}_{\phi_{\epsilon_\perp}}(\vec{x}, \vec{\rho}) = \frac{\mathcal{F}^{-1}\left(2\left\langle \Re\left(\mathcal{F}(\phi_{\epsilon_\perp}^2 P)\mathcal{F}^*(P)\right) - \mid \mathcal{F}(\phi_{\epsilon_\perp} P)\mid^2 \right\rangle\right)}{\mathcal{F}^{-1}\left(\mid \mathcal{F}(P)\mid^2\right)} \tag{12}$$

where $Cor(f, g) = \int f(x).g(x + \rho)dx$, $\mathcal{F}$ is the Fourier transform, $\mathcal{F}^{-1}$ the inverse Fourier transform, $\Re$ the real part of a complex value and * its conjugate. The phase screens being computed for $D/r_0 = 1$, the previous equation is scaled by a factor $(D/r_0)^{5/6}$, where the r_0 value is taken in the scientific image FITS header (Fusco et al., 2004).

2.4 Computation of the reconstructed OTF

Equation 1 actually does not take into account the hidden aberrations of the non-common path, i.e. the aberrations introduced by optical elements between the separating plate and the detector and hence non seen by the wavefront sensor (WFS). This equation should then be rewritten:

$$\left\langle OTF(\vec{\rho}/\lambda) \right\rangle = \left\langle OTF_{\phi_\epsilon}(\vec{\rho}/\lambda) \right\rangle \times OTF_{\mathrm{hid}}(\vec{\rho}/\lambda) \tag{13}$$

To calibrate these aberrations, one can use the acquisition of a point-source and the estimation of its long-exposure OTF due to the partial correction of AO:

$$\left\langle OTF^s(\vec{\rho}/\lambda) \right\rangle = \left\langle OTF_{\phi_\epsilon}^s(\vec{\rho}/\lambda) \right\rangle \times OTF_{\mathrm{hid}}^s(\vec{\rho}/\lambda) = \exp\left(-\frac{1}{2}\bar{D}^s{}_{\phi_\epsilon}(\vec{\rho})\right) \times OTF_{\mathrm{hid}}^s(\vec{\rho}/\lambda) \tag{14}$$

The reconstructed OTF of any AO image is then computed as follows:

$$\left\langle OTF(\vec{\rho}/\lambda) \right\rangle = \left\langle OTF^s(\vec{\rho}/\lambda) \right\rangle \times \exp\left(-\frac{1}{2}\left(\bar{D}_{\phi_\epsilon}(\vec{\rho}) - \bar{D}^s{}_{\phi_\epsilon}(\vec{\rho})\right)\right) \tag{15}$$

In the previous equation, $\bar{D}_{\phi_\epsilon}(\vec{\rho})$ and $\bar{D}^s{}_{\phi_\epsilon}(\vec{\rho})$ are estimated as described in Sect.2.2 and 2.3, and $\left\langle OTF^s(\vec{\rho}/\lambda) \right\rangle$ is directly computed from the image of the point-source.

3. FIRST RESULTS OF RECONSTRUCTION TESTS WITH NACO

Up until September 2007, two on-sky tests were performed, the results of which are reported below. Since then, the NACO software has been updated to provide the vector of Zernike variances as a FITS extension of the image FITS file. This will give us a much larger set of data on which to test PSF reconstruction. In the following we first describe a preliminary experiment to calibrate the reconstructed PSF orientation and then present the results of the on-sky tests.

3.1 Reconstructed PSF orientation calibration

In order to check for the orientation of reconstructed PSFs with respect to the corresponding CONICA images we have undertaken with the Paranal NACO team the following technical test:

1. close the AO loop on the internal NAOS fibre source and record slopes, voltages and offset voltages,

2. create from these data different sets of voltages, each set corresponding to a calibrated aberration,

3. apply in open loop these voltages on NACO and record the corresponding fibre images,

4. compare these NACO images to the images expected for the calibrated aberrations.

In practice, for a given set of voltages, the calibrated aberrations have been created by translating into voltages an additional positive or negative contribution of a single NAOS mode. Fig. 1 shows both the expected and observed fibre images for NAOS modes #5 and #6: the expected and observed images match well and there is no rotation or symmetry that could give the same matching.
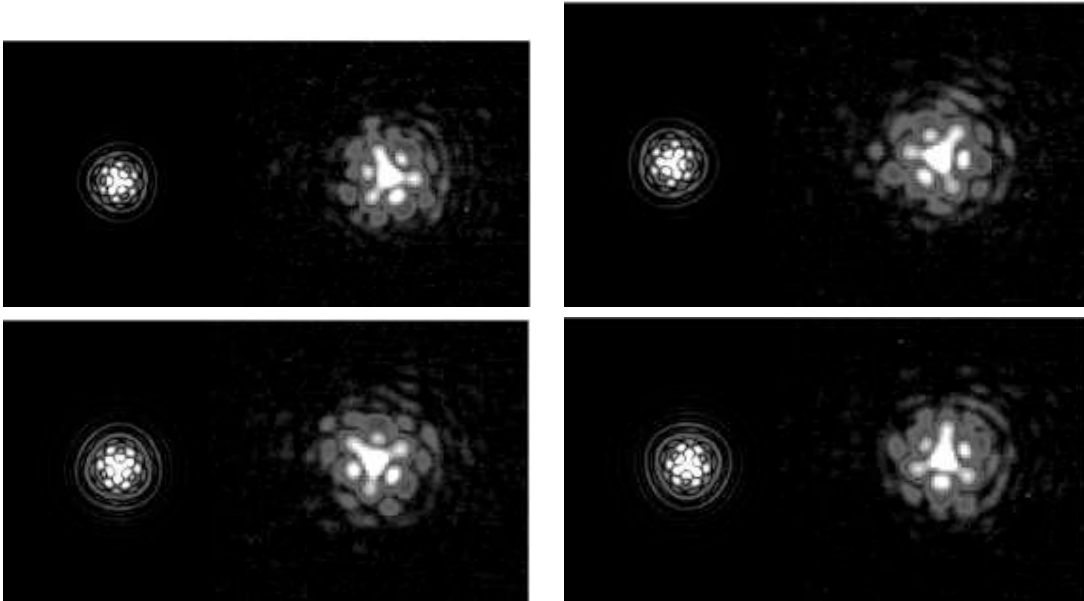

Figure 1. Comparison between expected and observed images obtained after the application of calibrated sets of voltages. Upper left: negative contribution of the NAOS mode #5. Upper right: positive contribution of the NAOS mode #5. Lower left: negative contribution of the NAOS mode #6. Lower right: positive contribution of the NAOS mode #6.

Fig. 2 shows both the expected and observed fibre images for "tip-tilt "NAOS modes and Table 1 gives the expected and observed (x,y) offsets when applying these modes. The latter were close to the former. The deviations between them could come either from a difference between the actual NACO pupil and the pupil used to computed the expected images or from a difference between the initial voltage vector used to compute the calibrated aberrations and the one really used when observing the aberrated images.

As a result from this test, reconstructed PSFs should have an orientation very similar to their corresponding NACO images.

Table 1. Observed and expected offsets of the fibre image when applying tip/tilt NAOS modes

Applied NAOS modes	Observed x and y offsets (in pixels)	Expected x and y offsets (in pixels)
negative tip	7.9, 0.4	8.9, 1.0
positive tip	-8.0, -0.2	-8.9, -1.0
negative tilt	-0.1, -7.5	0.6, -8.9
positive tilt	-0.3, 7.9	-0.6, 8.8
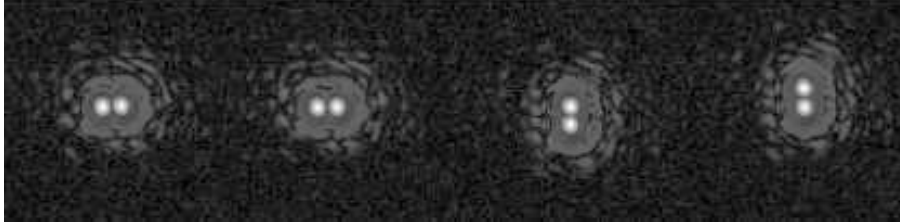
Figure 2. Observed images obtained after the application of calibrated sets of voltages. From left to right: negative "tip" NAOS mode contribution, positive "tip" NAOS mode contribution, negative "tilt" NAOS mode contribution, positive "tilt" NAOS mode contribution. Each image is actually the absolute value of the subtraction between the image obtained after the voltage application and the image without voltage application.

3.2 First on-sky test with NACO

The first on-sky test of PSF reconstruction with NACO has been done in November 2006. It consisted in the acquisition of five NACO images of a V=9 star (HD 8864), each acquisition being the result of 2 NDIT of DIT=5s. Atmospheric conditions were good: seeing of $\sim$0.5", $\tau_0\sim$7s and $r_0\sim$20cm, the latter two parameters being estimated by the RTC at λ=0.5μm (Fusco et al., 2004).

The PSF has been reconstructed using the V_{ii} algorithm and the covariance matrix $\langle \epsilon_\parallel \epsilon_\parallel{}^t \rangle$ has been computed only taking into account the corresponding measured residual covariance matrix $\langle \hat{\epsilon}_\parallel \hat{\epsilon}_\parallel^t \rangle$: the noise part was negligible for this (bright) star and the algorithm to computed the aliasing part was not available then. The non-common path aberrations were calibrated by using an image of the internal NAOS fibre source.

A comparison between the reconstructed and the observed PSFs is showned in Fig. 3. The Strehl ratio of the former is $\sim$39% whereas the one of the latter is $\sim$31%. The magnitude difference between the two PSFs, which provides an estimation of the photometric accuracy of the reconstruction, increases from $\sim$0.1 to $\sim$0.2 mag for radius between 0.1" (8 pixels) and 0.5" (40 pixels).
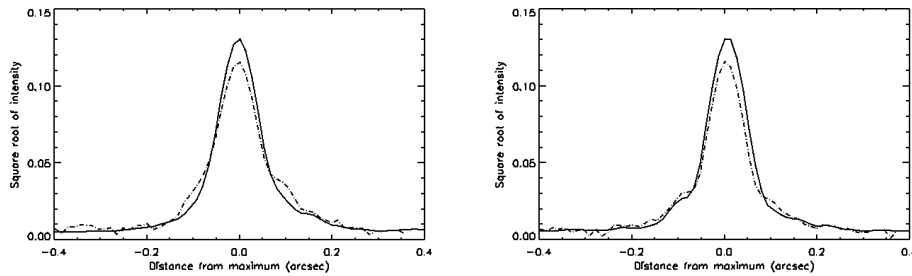

Figure 3. X-(left) and Y-(right) cuts of the reconstructed (plain line) and observed (dashed line) PSFs.

The discrepancies between the reconstructed and observed PSFs could be due to the presence of a faint (ΔK$\sim$3) companion close to the target (0.49", cf. Fig. 4), the lack of the aliasing contribution or/and the use of a fibre image instead of a bright star to calibrate the non common path aberrations, the latter being more accurate compared to the former.
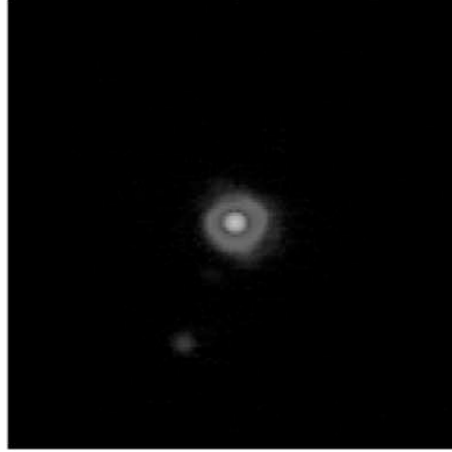
Figure 4. 1.7"×1.7" field image around the target.

3.3 Second on-sky test with NACO

The second on-sky test of PSF reconstruction with NACO has been done in September 2007. It consisted in the acquisition of:

- a test star: four NACO images of a V=12.7 star (S813-D), each acquisition being the result of 6 NDIT of DIT=20s, in the "2-3" visible WFS configuration (14×14 subapertures, 120 Hz),

- a non-common path aberration calibration star: six NACO images of a V=9.9 star (HD 194107), each acquisition being the result of 5 NDIT of DIT=4s, in the "2-2" visible WFS configuration (14×14 subapertures, 240 Hz).

Atmospheric conditions were good: seeing of ∼0.7", τ_0 between 4s and 6s and r_0 between 14 cm and 23cm, the latter two parameters being estimated by the RTC at λ=0.5μm (Fusco et al., 2004).

The PSF has been reconstructed using the V_{ii} algorithm and the covariance matrix $\langle \epsilon_\parallel \epsilon_\parallel^t \rangle$ has been computed taking into account the corresponding measured residual covariance matrix $\langle \hat{\epsilon}_\parallel \hat{\epsilon}_\parallel^t \rangle$ as well as the noise and aliasing contributions. Note that the noise contribution has been estimated from the so-called Zernike mean noise value originally delivered in the NACO image FITS header: the RTC software modification to provide the whole vector of Zernike variances has been done after this test.

A comparison between the reconstructed and the observed PSFs is showned in Fig. 4. The Strehl ratio of the former was ∼19% where as the one of the latter was ∼32%. The reconstruction was worse than for the first test. This discrepancy could be explained by an error in our estimation of the aliasing contribution or/and a bad estimation of the noise contribution using the Zernike mean noise value. Note also that this test star might have been too faint to provide a good reconstruction with such kind of algorithm.

4. PSF RECONSTRUCTION TESTS ON THE SÉSAME AO BENCH

4.1 The Sésame AO bench and its settings for our PSF reconstruction tests

Sésame is an optical bench developed at LESIA/Observatoire de Paris (PI: E. Gendron, project manager: Z. Hubert) for research and development studies in all fields connected to adaptive optics and more generally high angular resolution. This AO bench is a national facility and then open to the French high angular resolution community. It is designed to easily host external experiments needing an AO corrected turbulent beam, simulating a ground telescope.

Following the light path, Sésame design is as follows:

- light sources simulating stars (i.e. point-sources) or extended sources (few arcseconds) located at infinite distance or at a finite distance (90 km or more to simulate a laser source).
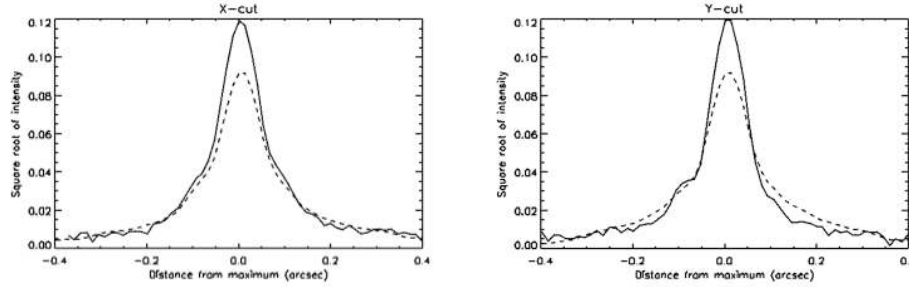
Figure 5. X-(left) and Y-(right) cuts of the reconstructed (plain line) and observed (dashed line) PSFs.

- a turbulence generator made of up to three motorised phase screens (in reflection or in transmission), which simulates the spatial and temporal behaviour of the atmospherical turbulence layers. The dynamical behaviour of the turbulence is simulated by rotating the phase screens, hence creating a "wind" moving a frozen turbulence (Taylor hypothesis). The rotation of the phase screens can be synchronised with the WFSs and "imaging" cameras to optimise the temporal aspects of the system. The location of the phase screens are determined by the turbulence layer altitude one wants to simulate.

- a 31 actuator bimorph deformable mirror (DM) installed in a MACAO-like tip-tilt mount (Arsenault et al., 2003). The parallel beam is in normal incidence on the DM surface and is injected thanks to a semi-reflecting beam splitter plate.

- several beam splitter plates to inject the beam to the hosted experiments.

- up to four 14×14 subaperture Shack-Hartmann WFSs.

For our PSF reconstruction tests, we have used Sésame in the following settings:

- a point-source located at infinite distance, at $\lambda = 620 \ nm$,

- one single phase screen in transmission simulating turbulence in the pupil at the ground level, with $D/r_0 = 9$ and a wind speed of $10 \ m/s$,

- the WFS and "imaging" camera acquisitions have been synchronised with the phase screen rotation so that to simulate a 100 Hz loop frequency and either one or two frame loop delay.

4.2 Results

For both one frame and two frame loop delay cases, we have recorded during a first phase screen rotation the slope and voltage measurements ("circular buffers") and the resulting images to derive the non-common path calibration image. Then, during a second phase screen rotation, we have added in the loop control software white noise to the slope measurements and recorded the new slope/voltage measurements and resulting images. In practice, the rms values of the measured slopes have been multiplied by a factor ∼1.5 when adding this white noise. Adding this random noise resulted in a degradation of the correction. It is this degraded point-source image we have reconstructed from Eq. 14.

Since we have used the same phase screen for the calibration image and the image to reconstruct, the reconstruction does not depend anymore on the aliasing and on the perpendicular part of the part: their contributions are the same for both images and eliminate themselves in Eq. 14. Then, only the measurement and the noise parts contribute to the mean structure function of the residual phase.

We show in Fig. 6 the resulting profiles of the different PSFs:

- the "observed" PSF;

- the PSF reconstructed with the noise estimated from the Zernike noise variance vector: the slope noise variance, assumed identical for all subapertures, is computed as the averaged of the vector made of the elements $\dfrac{n_{z_i}^2}{\displaystyle\sum_j M_{SZ_{i,j}}^2}$, where $n_{z_i}^2$ are the elements of the Zernike noise variance vector (computed from the auto-correlation of the reconstructed open-loop slope measurements projected on the Zernike basis) and M_{SZ}^2 is the "slope to Zernike" matrix,

- the PSF reconstructed with the "true" noise: the slope noise variance vector is computed directly from the slope measurements.

For the reconstructed PSFs, whatever the slope noise variance computation method, the modal noise covariance matrix $\langle nn^t \rangle$ is computed from :

$$\langle nn^t \rangle = M_{SM}\langle n_{s_i}n_{s_i}\rangle M_{SM}^t \tag{16}$$

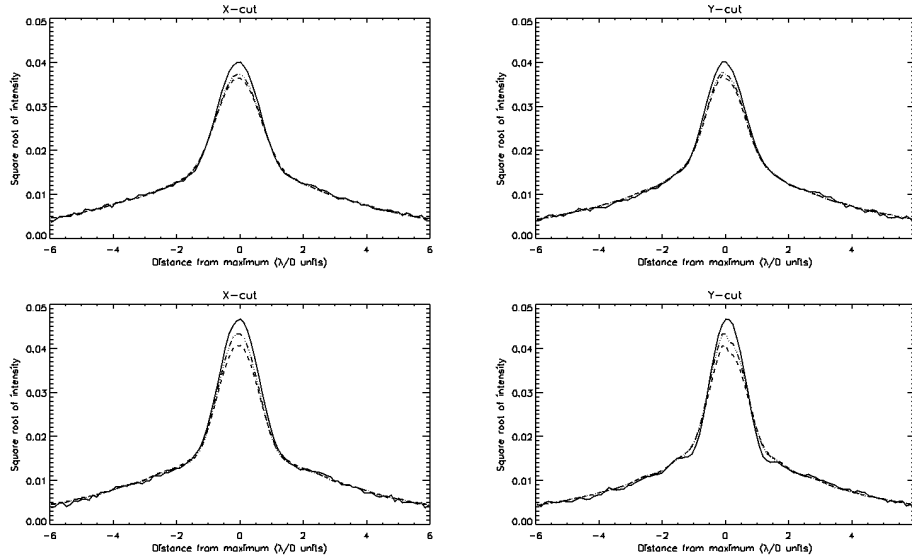where M_{SM} is the "slope to mode" matrix.

Figure 6. X-(left) and Y-(right) cuts of the "observed" (plain line), reconstructed (dashed lines) PSFs in the one frame (lower plots) and two frame (upper plots) delay settings. The "short" dashed line curves represents the PSFs reconstructed with the noise estimated from the Zernike noise variance vector whereas the "long" dashed lines curves represents the PSFs reconstructed with the "true" noise, computed directly from the slope measurements ("circular buffer").

These plots demonstrate that:

- the loss of accuracy is weak when estimating the noise from the Zernike noise variance vector, but this has to be confirmed with a stronger degradation of the correction,

- the structures in the PSF wings are not perfectly reproduced in the reconstructed PSFs: this is probably due to the fact that the latter corresponds to infinitely long exposures whereas the "observed" PSFs are obtained after a finite exposure time, that is probably not long enough since speckle structures can still be observed in the image (the phase screen does not allow one to integrate over a larger number of iterations),

- even if it good, the reconstructions are not perfect: the most probable origin of this discrepancy is the too low loop frequency we used for this test. At 100 HZ, the high WFS bandpass is probably not valid and the model inaccurate.

5. CONCLUSION

The PSF reconstruction tests undertaken with NACO have lead to unsatisfactory results. Though, they have been undertaken when all the tools of our algorithm were not available: we still have not tested a reconstruction with the entire vector of Zernike noise variance.

To less depend on the availability of NACO for these PSF reconstruction data acquisition and to test the different counterparts of the reconstruction, we have just begun to use the Sésame AO bench to test our algorithm. First results are promising but need to be confirmed with more additional atmospherical conditions and correction qualities.

References

Arsenault, R., Alonso, J., Bonnet, H., Brynnel, J., Delabre, B., Donaldson, R., Dupuy, C., Fedrigo, E., Farinato, J., Hubin, N., Ivanescu, L., Kasper, M., Paufique, J., Rossi, S., Tordo, S., Stroebele, S., Lizon, J.-L., Gigan, P., Delplancke, F., Silber, A., Quattri, M., Reiss, R. 2003, Proc. SPIE, 4839, 174

Clénet, Y., Kasper, M., Gendron, E., Fusco, T., Rousset, G., Gratadour,, D., Lidman, C., Marco, O., Ageorges, N., Egner, S. 2006, Proc. SPIE, 6272, 62723T-1–62723T-12

Fitzgerald M. 2004, in "The 1st Victoria Workshop on AO-PSF reconstruction", L. Jollissaint and J.-P. Véran and J. Christou and T. Rimmele ed., http://cfao.ucolick.org/meetings/psf_reconstruction

Flicker, R., Le Mignant, D. 2008, Proc. SPIE, this volume

Fusco, T., Rousset, G., Rabaud, D., et al. 2004, J. Opt. A: Pure Appl. Opt., 6, 585

Gendron, E., Clénet, Y., Fusco, T., Rousset, G. 2006, A&A, 457, 359

Harder, S., & Chelli, A. 2000, A&AS, 142, 119

Jolissaint, L., Véran, J.-P., Marino, J. 2004, Proc. SPIE, 5490, 151

Véran, J.-P., Rigaut, F., Maître H., Rouan, D. 1997, Journal of the Optical Society of America A, 14, 3057

Weiss, R. 2003, PhD Thesis, Naturwissenschaftlich-Mathematische Gesamtfakultät der Universität Heidelberg, Germany